

# Bridging Quantum Computing and Nuclear Structure: Atomic Nuclei on a Trapped-Ion Quantum Computer

Sota Yoshida\*

*School of Data Science and Management, Utsunomiya University, Mine, Utsunomiya, 321-8505, Japan and  
RIKEN Nishina Center for Accelerator-based Science, RIKEN, Wako 351-0198, Japan*

Takeshi Sato

*Graduate School of Engineering, The University of Tokyo,  
7-3-1 Hongo, Bunkyo-ku, Tokyo 113-8656, Japan  
Photon Science Center, School of Engineering, The University of Tokyo,  
7-3-1 Hongo, Bunkyo-ku, Tokyo 113-8656, Japan and  
Research Institute for Photon Science and Laser Technology,  
The University of Tokyo, 7-3-1 Hongo, Bunkyo-ku, Tokyo 113-0033, Japan*

Takumi Ogata

*Graduate School of Engineering, The University of Tokyo,  
7-3-1 Hongo, Bunkyo-ku, Tokyo 113-8656, Japan*

Masaaki Kimura

*RIKEN Nishina Center for Accelerator-based Science, RIKEN, Wako 351-0198, Japan*

We report accurate quantum simulations of medium-mass atomic nuclei—including oxygen, calcium, and nickel—on the RIKEN–Quantinuum Reimei trapped-ion quantum computer, achieving sub-percent accuracy. Using a symmetry-aware pair-unitary coupled-cluster doubles (pUCCD) ansatz implemented with a hard-core-boson mapping, and with particle-number-restoring post-selection, our ground-state energy estimates agree with noise-free statevector simulations and with exact diagonalization results on the order of 0.1% relative error. These experiments establish a new benchmark for quantum simulations of strongly correlated nuclear systems on real hardware and demonstrate the near-term potential of high-fidelity trapped-ion platforms for nuclear-structure calculations.

## INTRODUCTION

Quantum simulation of many-body systems is a leading application of quantum computing, with potential impact across quantum chemistry, condensed-matter physics and nuclear physics. While quantum algorithms and hardware have advanced rapidly, demonstrating clear advantage for interacting many-body problems remains an open challenge. For example, a recent study [1] identified scenarios in which quantum devices can outperform classical algorithms for certain spin models. Nonetheless, general claims of quantum advantage for many-body systems remain inconclusive and require careful, system-specific analysis.

On near-term devices, variational approaches such as the Variational Quantum Eigensolver [2, 3] rely crucially on the choice of an ansatz that balances implementability and expressivity. Common families of ansätze — including unitary coupled cluster (UCC) variants — can be effective in some domains but often suffer from optimization difficulties, called barren plateaus [4], or unfavorable scaling of parameters and gate depth as system size grows. This situation has evoked a broader consideration of quantum algorithms beyond NISQ towards

fault-tolerant quantum computing (FTQC), leading to a term like Early Fault-Tolerant Quantum Computing (E-FTQC) [5].

In such situations, it is essential to broadly examine each component of quantum computation—namely, state preparation (also simply called the ansatz), the circuit for executing quantum algorithms, and the measurement strategy for evaluating the observable of interest—for each specific problem. The first part, the choice of the ansatz, plays a central role in any quantum algorithm. Even for fault-tolerant quantum computing (FTQC) approaches, such as Quantum Phase Estimation (QPE)[6] and early-FTQC algorithms [5], state preparation remains a fundamental building block for quantum algorithms. This is because the success of the quantum algorithm largely depends on the quality of the prepared quantum state, i.e., the overlap between the prepared state and the target state. In spin systems or chemical systems, various ansätze have been proposed, such as UCC-family, and ones based on matrix product states or tensor network states more generally [7–9].

Compared to other areas tackling quantum many-body problems, nuclear physics studies have seen relatively limited applications of quantum computing, despite several pioneering works [10–12], and recent reviews [13, 14]. In addition, only a few ansätze have been explored for nuclear systems, almost exclusively based on the uni-

\* syoshida@a.utsunomiya-u.ac.jp

tary coupled cluster (UCC) family [12, 15, 16] with some variations such as Adapt-VQE [17]. A seminal work investigated the applicability of the UCC + Adapt-VQE to the nuclear shell model [12], where the number of CNOT gates required to achieve a given accuracy for shell-model calculations of oxygen and calcium isotopes was estimated.

Nuclear many-body systems are distinguished from other quantum many-body systems by exceptionally strong correlations arising from the nature of nuclear forces, posing a unique challenge for both classical and quantum computing. Even in the low-energy regime, where nucleons are the only explicit baryonic degrees of freedom, the problem is complicated by the fact that protons and neutrons—fermions of nearly equal mass—interact through multiple channels in an intricate manner. This results in a large number of non-negligible Hamiltonian terms and strong non-locality. Furthermore, anisotropic components of the interaction, such as tensor forces [18] and three-body forces [19], play an essential role in describing the rich phenomena of nuclear systems. These features are generally difficult to capture with a simple wave-function ansatz. Another manifestation of this complexity is entanglement entropy, which in nuclear systems obeys a volume law rather than an area law [20], hindering straightforward application of tensor networks, although extensions of tensor-network methods to such systems remain a promising direction [21–23].

Consequently, most quantum-computing studies of nuclear structure have focused on small systems or relied on classical simulators. Reported errors in ground-state energies range from 4 ~ 13% for  ${}^6\text{Li}$  [15] and 3 ~ 13% for oxygen isotopes [16]. In our previous work [24], we achieved relative errors below 0.1% for  ${}^6\text{He}$  and  ${}^{18}\text{O}$ , and about 1% for  ${}^{42}\text{Ca}$  on an IBM superconducting quantum device. However, those target systems were limited to valence two-neutron configurations and may not be scalable to heavier nuclei.

In this work, we introduce a hard-core-boson (HCB) mapping of the nuclear shell model combined with the pair-unitary coupled-cluster doubles (pUCCD) ansatz, which efficiently captures strong pairing correlations between nucleons of the same species. While pUCCD ansatzes have been shown to be effective for chemical systems [25–27], this study reports, to our knowledge, the first demonstration of pUCCD applied to nuclear many-body systems on a quantum device. Implemented on the high-fidelity trapped-ion processor RIKEN–Quantinuum Reimei, and augmented by symmetry-aware ansatzes and post-selection techniques, our approach yields ground-state energies for oxygen, calcium, and nickel isotopes that agree with noise-free statevector simulations within sub-percent relative error. These results establish a new experimental benchmark for quantum simulations of strongly correlated nuclear systems and demonstrate the near-term potential of trapped-ion platforms for nuclear-structure calculations.

## RESULTS

In this section, we present the results of the pUCCD ansatz on the Reimei quantum hardware for the ground-state energies of oxygen, calcium, and nickel isotopes. The Reimei is based on Quantinuum’s H-1 series trapped-ion quantum computer, and has 20 qubits with all-to-all connectivity. The Reimei device is installed in RIKEN’s Wako campus, and started its operation in February 2025. Calculations are performed via Nexus [28], a cloud-based quantum computing platform provided by Quantinuum enabling users to run quantum simulations on various backends, including noise-free statevector simulators, emulators, and real devices.

### Target systems

In this work, we study even-neutron isotopes of oxygen, calcium, and To demonstrate the capability of our approach, we focus on oxygen, calcium, and nickel isotopes, which span light to medium-mass nuclei and serve as standard benchmarks in nuclear structure calculations. The corresponding valence spaces are restricted to  $sd$ ,  $pf$ , and  $jj45$  shells, respectively, allowing feasible implementations on classical/quantum hardware and direct comparison with classical exact diagonalization.

As detailed in Methods section, we adopt the so-called pair unitary coupled cluster doubles (pUCCD) ansatz by folding the Fermionic degrees of freedom into Hard-core boson (HCB) degrees of freedom. The resulting qubit Hamiltonian takes the form:

$$H_{\text{qubit}} = \sum_i \frac{\varepsilon_i + V_{ii}}{2} (I_i - Z_i) + \frac{1}{4} \sum_{i \neq j} V_{ij} (X_i X_j + Y_i Y_j) + \frac{1}{4} \sum_{i \neq j} V_{ij}^m (I_i - Z_i)(I_j - Z_j), \quad (1)$$

where  $i$  denotes the pair index of single-particle states in the valence space specified by  $n$  (principal quantum number),  $l$  (orbital angular momentum),  $j$  (total angular momentum),  $|j_z|$  (absolute value of the angular momentum projection on the  $z$ -axis), and  $t_z$  (isospin projection) quanta.

All terms of the Hamiltonian Eq. (1) except the second are diagonal in the computational basis and can be measured directly by measuring the expectation values of the Pauli-Z operators. For the non-diagonal  $XX + YY$  terms, we employed two strategies. The first, called “Hadamard”, uses Hadamard gates to measure  $\langle XX \rangle$ , from which  $\langle YY \rangle$  follows by symmetry. The second, called “Basis rotations”, applies a basis rotation to diagonalize  $XX + YY$  in the computational basis; for this strategy, we additionally post-selected bitstrings to restore particle-number symmetry. More details on the measurement are provided in the Methods section.

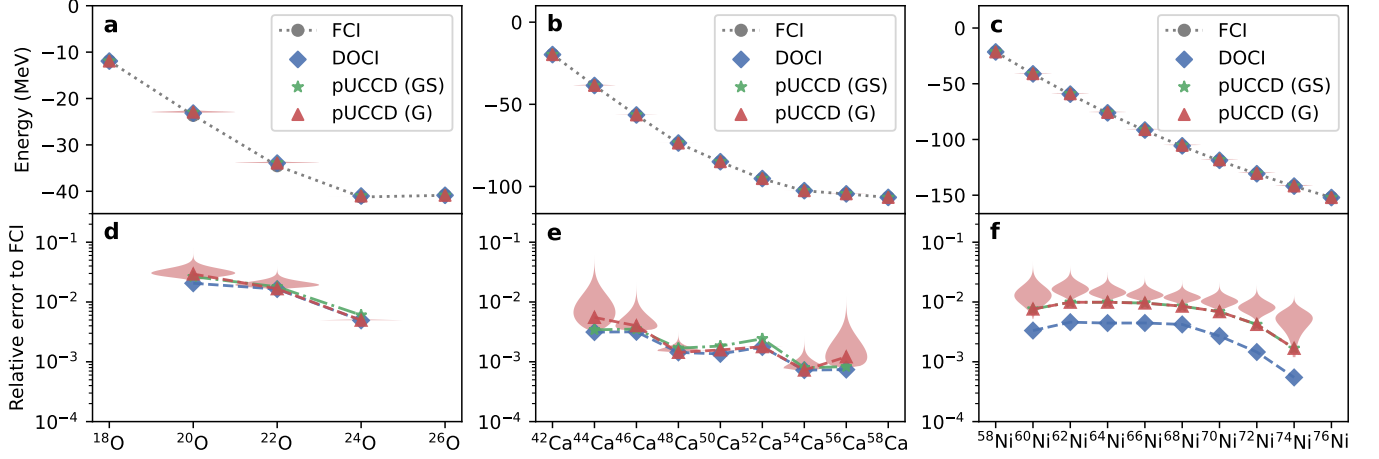


FIG. 1. **Ground-state energies of target isotopes on noise-free statevector simulators.** **a–c** Full configuration interaction (FCI, dotted lines with gray circles) and doubly occupied configuration interaction (DOCI, blue diamonds) are compared with statevector simulations using the pUCCD (GS) ansatz (green stars) and the pUCCD (G) ansatz (red triangles). Here, pUCCD (GS) denotes the pUCCD ansatz implemented with nearest-neighbor Givens rotations and SWAP gates, while pUCCD (G) assumes all-to-all connectivity, as realized in the Reimei device. **d–f** Differences between the pUCCD ansatz results and the DOCI results are shown relative to FCI in logarithmic scale. Uncertainty bands for pUCCD (G) are obtained by random sampling over circuits with different initial configurations and Givens-rotation orderings.

### Ideal simulation results of the pUCCD ansatz

We first assess the performance of the pUCCD ansatz on a noiseless statevector simulator, thereby probing its intrinsic accuracy. As a baseline, Full Configuration Interaction (FCI) provides the exact ground-state energies within the valence space. DOCI provides the exact solution within the zero-seniority space, whereas pUCCD offers a compact exponential parametrization of this space, and thus approximates DOCI. Therefore, any deviation from the FCI results reflects the intrinsic limitations of the ansatz itself, independent of hardware noise or statistical noise arising from the limited number of measurement shots.

In what follows, we consider two types of pUCCD ansatz, named pUCCD (GS) and pUCCD (G). The (GS) represents Givens plus SWAP, which consists of only nearest neighbor Givens rotations and thereby more suitable for hardware with a limited connectivity [25, 29]. On the other hand, (G) stands for Givens rotations where all-to-all connectivity is assumed. In experiments on the Reimei device, we will focus on the pUCCD (G) ansatz. For more details of ansatz design, see Methods section.

Fig. 1 shows ground-state energies for the target isotopes, obtained with pUCCD (G), pUCCD (GS), DOCI, and FCI on noise-free statevector simulators. At this scale, all curves are nearly indistinguishable, and the lower panels therefore highlight relative deviations from FCI on a logarithmic scale. Results for two-neutron (or two-neutron-hole) systems are omitted, since both DOCI and pUCCD exactly reproduce FCI in those cases.

For the pUCCD ansatz, the symbols show the results of one representative realization of the ansatz, and the

uncertainty bands are plotted for the pUCCD (G) ansatz by random sampling of the circuit with different reference states and order of Givens rotations. The detailed explanation of the uncertainty bands is given in Supplementary Information.

Most importantly, pUCCD reproduces DOCI energies with an error of less than 1%, while using far fewer parameters, demonstrating its compact yet accurate description. For reference, DOCI itself reproduces FCI ground-state energies within 0.1 – 1%, with deviations smaller than the typical uncertainties (a few percent) of modern nuclear many-body methods [30]. The residual differences depend on the target system: Ca isotopes in the  $pf$  shell are well described within the zero-seniority space (DOCI), whereas oxygen isotopes show larger contributions from higher-seniority configurations, leading to slightly larger deviations from FCI.

Nickel isotopes in the  $jj45$  shell exhibit larger discrepancies between DOCI and pUCCD compared to oxygen and calcium isotopes. This arises from the factors intrinsic to the  $jj45$  shell. The valence space,  $jj45$  shell, consists of four  $jj$ -coupling orbitals ( $1p_{1/2}, 1p_{3/2}, 0f_{5/2}, 0g_{9/2}$ ), and the configuration mixing among these orbitals is pronounced in Ni isotopes even for ground states since their effective single particle energies are close to each other [31]. The single-Trotter pUCCD ansatz, while efficient for capturing pairing correlations, becomes less expressive in the presence of such strong configuration mixing.

TABLE I. **Summary of pUCCD results on the RIKEN–Quantinuum Reimei device.** The “FCI” column lists exact ground-state energies obtained with the full configuration interaction method in the original fermionic representation. The “Ideal pUCCD” column shows results from the pUCCD ansatz in the hard-core-boson formalism. The fourth and fifth columns show experimental results on the Reimei device using two different post-selection techniques. The numbers in parentheses indicate the relative errors with respect to the pUCCD statevector simulations. The last column gives the valid ratio, i.e., the fraction of measured bitstrings preserving the correct particle number of the target nucleus. All energies are in MeV.

| Nuclide          | FCI      | Ideal pUCCD | Reimei: Hadamard |                            | Reimei: Basis rotation |                            | Valid ratio |
|------------------|----------|-------------|------------------|----------------------------|------------------------|----------------------------|-------------|
| <sup>18</sup> O  | -11.932  | -11.932     | -11.802          | ( $1.1 \times 10^0\%$ )    | -11.893                | ( $3.3 \times 10^{-1}\%$ ) | 0.98        |
| <sup>20</sup> O  | -23.632  | -22.939     | -22.383          | ( $2.4 \times 10^0\%$ )    | -22.854                | ( $3.7 \times 10^{-1}\%$ ) | 0.98        |
| <sup>22</sup> O  | -34.498  | -33.924     | -33.560          | ( $1.1 \times 10^0\%$ )    | -33.829                | ( $2.8 \times 10^{-1}\%$ ) | 0.97        |
| <sup>24</sup> O  | -41.225  | -41.021     | -40.985          | ( $8.8 \times 10^{-2}\%$ ) | -41.027                | ( $1.5 \times 10^{-2}\%$ ) | 0.97        |
| <sup>26</sup> O  | -40.869  | -40.869     | -40.613          | ( $6.3 \times 10^{-1}\%$ ) | -40.940                | ( $1.8 \times 10^{-1}\%$ ) | 0.96        |
| <sup>42</sup> Ca | -19.734  | -19.734     | -19.727          | ( $3.6 \times 10^{-2}\%$ ) | -19.775                | ( $2.1 \times 10^{-1}\%$ ) | 0.97        |
| <sup>44</sup> Ca | -38.675  | -38.462     | -38.540          | ( $2.0 \times 10^{-1}\%$ ) | -38.424                | ( $9.9 \times 10^{-2}\%$ ) | 0.97        |
| <sup>46</sup> Ca | -56.667  | -56.440     | -56.414          | ( $4.7 \times 10^{-2}\%$ ) | -56.565                | ( $2.2 \times 10^{-1}\%$ ) | 0.96        |
| <sup>48</sup> Ca | -73.662  | -73.556     | -73.538          | ( $2.5 \times 10^{-2}\%$ ) | -73.489                | ( $9.1 \times 10^{-2}\%$ ) | 0.95        |
| <sup>50</sup> Ca | -85.055  | -84.921     | -85.135          | ( $2.5 \times 10^{-1}\%$ ) | -85.007                | ( $1.0 \times 10^{-1}\%$ ) | 0.94        |
| <sup>52</sup> Ca | -95.360  | -95.190     | -95.038          | ( $1.6 \times 10^{-1}\%$ ) | -95.149                | ( $4.3 \times 10^{-2}\%$ ) | 0.94        |
| <sup>54</sup> Ca | -102.632 | -102.557    | -102.622         | ( $6.3 \times 10^{-2}\%$ ) | -102.648               | ( $8.8 \times 10^{-2}\%$ ) | 0.94        |
| <sup>56</sup> Ca | -104.589 | -104.462    | -104.620         | ( $1.5 \times 10^{-1}\%$ ) | -104.325               | ( $1.3 \times 10^{-1}\%$ ) | 0.94        |
| <sup>58</sup> Ca | -106.666 | -106.666    | -106.885         | ( $2.0 \times 10^{-1}\%$ ) | -106.668               | ( $1.7 \times 10^{-3}\%$ ) | 0.94        |
| <sup>58</sup> Ni | -21.447  | -21.447     | -21.207          | ( $1.1 \times 10^0\%$ )    | -21.291                | ( $7.3 \times 10^{-1}\%$ ) | 0.93        |
| <sup>60</sup> Ni | -41.276  | -40.961     | -40.752          | ( $5.1 \times 10^{-1}\%$ ) | -40.992                | ( $7.4 \times 10^{-2}\%$ ) | 0.94        |
| <sup>62</sup> Ni | -59.602  | -59.013     | -58.703          | ( $5.2 \times 10^{-1}\%$ ) | -59.015                | ( $4.5 \times 10^{-3}\%$ ) | 0.93        |
| <sup>64</sup> Ni | -76.444  | -75.687     | -76.027          | ( $4.5 \times 10^{-1}\%$ ) | -75.765                | ( $1.0 \times 10^{-1}\%$ ) | 0.92        |
| <sup>66</sup> Ni | -91.941  | -91.059     | -90.552          | ( $5.6 \times 10^{-1}\%$ ) | -90.695                | ( $4.0 \times 10^{-1}\%$ ) | 0.93        |
| <sup>68</sup> Ni | -106.140 | -105.237    | -105.169         | ( $6.5 \times 10^{-2}\%$ ) | -105.288               | ( $4.8 \times 10^{-2}\%$ ) | 0.92        |
| <sup>70</sup> Ni | -119.034 | -118.215    | -118.189         | ( $2.2 \times 10^{-2}\%$ ) | -118.158               | ( $4.8 \times 10^{-2}\%$ ) | 0.91        |
| <sup>72</sup> Ni | -130.930 | -130.379    | -130.511         | ( $1.0 \times 10^{-1}\%$ ) | -130.397               | ( $1.3 \times 10^{-2}\%$ ) | 0.95        |
| <sup>74</sup> Ni | -141.932 | -141.694    | -141.565         | ( $9.1 \times 10^{-2}\%$ ) | -141.715               | ( $1.5 \times 10^{-2}\%$ ) | 0.93        |
| <sup>76</sup> Ni | -152.103 | -152.103    | -151.986         | ( $7.7 \times 10^{-2}\%$ ) | -152.054               | ( $3.2 \times 10^{-2}\%$ ) | 0.94        |

### Results on RIKEN–Quantinuum’s Reimei device

We next implement the pUCCD (G) ansatz on the Reimei trapped-ion quantum computer. Table I summarizes the hardware results of the pUCCD (G) ansatz together with ideal simulations by noise-free statevector simulators. The measured energies agree closely with the noise-free simulations, showing relative errors mostly below 0.3% and at most a few percent relative to FCI. These achievements represent the most accurate quantum-computing results for nuclear many-body ground states obtained on real devices to date.

Between the two measurement strategies, the basis-rotation method consistently outperforms the Hadamard method, yielding results closer to ideal simulations. This trend is further supported by bootstrapping analyses shown in Fig. 2. Lighter isotopes exhibit larger uncertainties because  $XX + YY$  terms, where the difference between the two measurement strategies lies, contribute more significantly to the total energy in lighter isotopes. In contrast, for heavier isotopes, the mass-dependent scaling commonly applied to two-body matrix elements in phenomenological shell-model interactions reduces the absolute size of the  $XX + YY$  contributions (e.g., TBMEs for <sup>58</sup>Ca and <sup>78</sup>Ni are multiplied by  $\sim 0.9$  compared with

<sup>42</sup>Ca and <sup>58</sup>Ni), which further diminishes their relative contribution to the total energy.

### DISCUSSION

Quantum many-body systems has become a central focus of quantum computing research over the past decade, driven by rapid progress in algorithms and hardware. However, demonstrating genuine quantum advantage in interacting many-body physics remains an open challenge, requiring advances in all components of the algorithmic workflow: ansatz design, measurement strategies, and optimization techniques. In this work, we concentrated on ansatz construction and measurement from the standpoint of nuclear structure, where exceptionally strong correlations make the choice of ansatz especially critical.

By combining a hard-core boson (HCB) mapping of the nuclear shell-model Hamiltonian with a pair-unitary coupled cluster doubles (pUCCD) ansatz, we demonstrated accurate ground-state calculations of oxygen, calcium, and nickel isotopes on the RIKEN–Quantinuum Reimei trapped-ion quantum computer. Our results achieve sub-percent agreement with noise-free statevec-



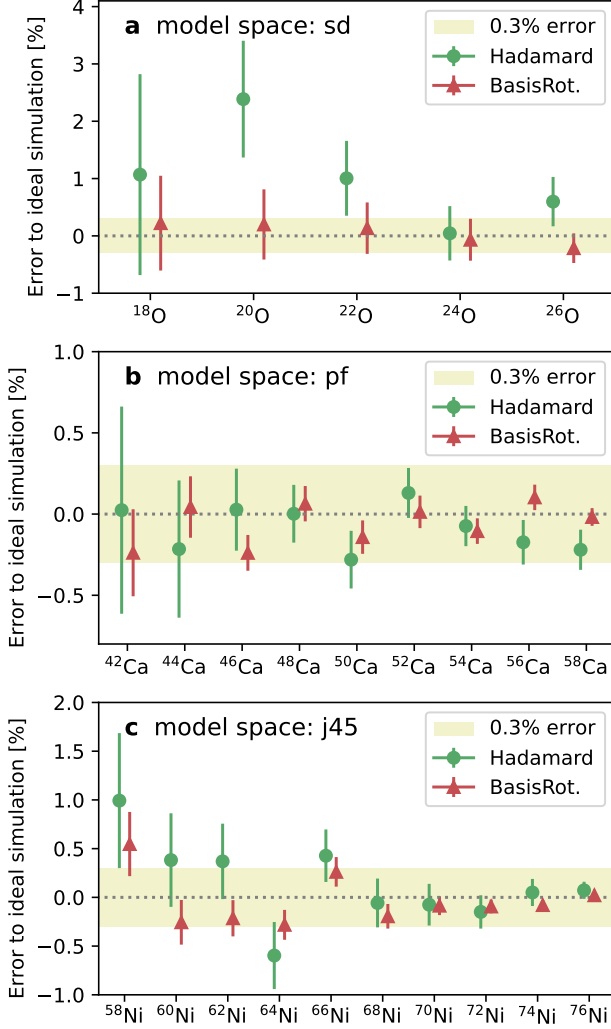


FIG. 2. **Ground-state energies of target isotopes on the RIKEN-Quantinuum Reimei device.** **a** oxygen, **b** calcium, **c** nickel isotopes. Energy estimates are shown relative to noise-free statevector simulations. The error bars represent statistical uncertainties, evaluated by bootstrapping with 500 resampling of datasets obtained from 1,024 measurement shots. The shaded band corresponds to a 0.3% relative error with respect to the statevector results; most data points fall within this range.

tor simulations and exact diagonalization results, setting a new benchmark for nuclear-structure simulations on real NISQ hardware.

Although the pUCCD parameters were optimized using a classical simulator, this proof-of-principle study highlights how physically motivated, compact ansatz can deliver accurate results with modest qubit numbers and circuit depths. Such strategies may guide the discovery of efficient variational forms for larger systems where classical pre-optimization is infeasible.

Looking ahead, incorporating proton-neutron interactions will require ansatz capable of describing more general non-local correlations. Nonetheless, the present

results demonstrate the viability of pUCCD for multi-neutron (or multi-proton) systems, and point toward applications to heavier systems such as neutron drops or neutron-rich isotopes. As an illustration of possible extensions, entropy-driven entanglement forging [32] has recently been proposed to localize correlations in Adapt-VQE circuits; similar ideas could be combined with pUCCD, for instance by monitoring generalized seniority.

Beyond ansatz design, new algorithmic paradigms merit exploration. Quantum subspace diagonalization techniques [33–37], including Quantum Krylov and related methods, use quantum devices to generate subspace states while delegating diagonalization to classical post-processing. These approaches provide access to excited states and transition properties such as electromagnetic transitions. Such hybrid methods, combined with compact ansatz like pUCCD, represent a promising path toward realistic quantum simulations of nuclear spectroscopy in the near future.

## METHODS

### Basis states and Hamiltonians

General Shell-model Hamiltonians with up to two-body interactions can be expressed as

$$\hat{H} = \sum_i h_{ij} a_i^\dagger a_j + \frac{1}{4} \sum_{ijkl} V_{ijkl} a_i^\dagger a_j^\dagger a_l a_k, \quad (2)$$

where  $i$  denotes the single-particle state characterized by the quantum numbers  $\{n, l, j, j_z, t_z\}$ . Here,  $n$  is the principal quantum number,  $l$  the orbital angular momentum,  $j$  the total angular momentum,  $j_z$  its projection of  $j$  onto the  $z$ -axis, and  $t_z$  the isospin projection.

or systems within one or two major shells, as in this work, the one-body term reduces to the diagonal form  $\varepsilon_i \equiv h_{ii}$ , called the single-particle energies (SPEs). The fermionic creation and annihilation operators,  $a_i^\dagger$  and  $a_i$ , act on these single-particle states, while  $V_{ijkl}$  denotes the two-body matrix elements (TBMEs).

These SPEs and TBMEs can be either derived from the realistic nucleon-nucleon interactions or from the phenomenological adjustments to reproduce experimental data for binding energies, excitation energies, and so on. The model space and adopted interactions in this work are summarized in Table II. The methods in this work can be applied to any other interactions including microscopically derived ones. Diagonalization with these interactions can be reproduced using publicly available codes such as KSHELL [38, 39] or NuclearToolkit.jl [40, 41].

Once the Hamiltonian is defined, one can diagonalize the Hamiltonian in a given model space, leading to the Configuration Interaction (CI) method. Here, "full configuration interaction" (FCI) refers to exact diagonaliza-

TABLE II. Adopted interactions and model spaces.

| Nuclide             | Interaction  | Model space   |
|---------------------|--------------|---|
| $^{18-26}\text{O}$  | USDB [42]    | $sd$ ( $1s_{1/2}, 0d_{3/2}, 0d_{5/2}$ )             |
| $^{42-58}\text{Ca}$ | GXPFI1A [43] | $pf$ ( $1p_{1/2}, 1p_{3/2}, 0f_{5/2}, 0f_{7/2}$ )   |
| $^{58-76}\text{Ni}$ | JUN45 [31]   | $jj45$ ( $1p_{1/2}, 1p_{3/2}, 0f_{5/2}, 0g_{9/2}$ ) |

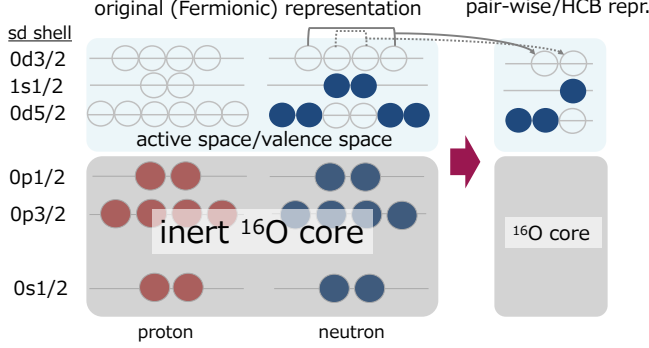


FIG. 3. **Schematics of the hard-core boson (HCB) representation.** This example shows a configuration of  $^{22}\text{O}$  nucleus on top of the inert core  $^{16}\text{O}$ . The active (valence) space consists of  $1s_{1/2}$ ,  $0d_{3/2}$ , and  $0d_{5/2}$  single-particle states.

tion within the selected valence space, following the convention of quantum chemistry (rather than the no-core shell model definition often used in nuclear physics).

A useful truncation of CI is the doubly occupied configuration interaction (DOCI) method, equivalent to restricting the shell-model space to zero-seniority configurations, i.e., considering only time-reversed nucleon pairs as active degrees of freedom. In even-neutron systems, DOCI often provides a good approximation to FCI and is exact for two-valence-neutron  $J = 0$  states. This DOCI method has been also used in nuclear physics and proven to be a good approximation to even-number neutron systems [44]. Thus, DOCI serves as an important benchmark in this work.

Another viable method for approximating FCI and/or DOCI is the use of pair coupled cluster methods and their extensions [25–27, 45–47]. Whereas the methods have been successfully applied to pairing Hamiltonians (also known as BCS Hamiltonians) in the nuclear physics context, their applications to more general shell-model Hamiltonians remain limited and warrant further exploration.

It should also be noted that the way to represent the Hamiltonian in paired form is not unique, and the choice of the pairs can be different depending on the context. In the case of electronic structure calculations, the natural assumption is to consider the spin up and spin down electrons as a pair. Detailed derivations of the zero-seniority Hamiltonian for electronic structure calculations can be found in e.g. [46]. For nuclear many-body methods one has more freedom involved in the system, and one can consider the pairs of nucleons with different spins and/or

different orbitals.

Fig. 3 shows the schematic figure of the hard-core boson (HCB) representation, which is a core assumption in this work for describing target systems efficiently. As an example, the figure shows a configuration of  $^{22}\text{O}$  nucleus on top of the inert  $^{16}\text{O}$  core. The single-particle states are specified by the quantum numbers  $\{n, l, j, j_z, t_z\}$ , leading to 12 single-particle states for both protons and neutrons in the  $sd$  shell.

Within the zero-seniority approximation, the active degrees of freedom can be restricted to time-reversal pairs of nucleons (neutrons in this case). Consequently, the number of qubits required to represent the system is reduced to half the number of single-particle states in the original fermionic representation.

In the HCB representation, the Hamiltonian becomes

$$H = \sum_{i < 0} \varepsilon_i (a_i^\dagger a_i + a_{\bar{i}}^\dagger a_{\bar{i}}) + \sum_{i < 0} V_{i\bar{i}\bar{i}i} a_i^\dagger a_{\bar{i}}^\dagger a_{\bar{i}} a_i + \sum_{i \neq j < 0} V_{i\bar{i}j\bar{j}} a_i^\dagger a_{\bar{i}}^\dagger a_{\bar{j}} a_j + \frac{1}{4} \sum_{i, j \notin \{i, \bar{i}\}} V_{ijij} n_i n_j, \quad (3)$$

where  $i < 0$  denotes single-particle states with negative  $j_z$  values, and  $\bar{i}$  is the time-reversal partner of the single-particle state  $i$ . The last term, absent in the valence two-neutron systems studied previously [24], can be regarded as a mean-field contribution from other occupied pairs.

Defining pair creation, annihilation, and occupation operators,

$$A_i^\dagger = a_i^\dagger a_{\bar{i}}^\dagger, \quad (4)$$

$$A_{\bar{i}} = a_{\bar{i}} a_i, \quad (5)$$

$$N_{\bar{i}} = \frac{1}{2}(n_i + n_{\bar{i}}) = \frac{1}{2}(a_i^\dagger a_i + a_{\bar{i}}^\dagger a_{\bar{i}}), \quad (6)$$

the Hamiltonian can be rewritten in pairwise or hard-core boson (HCB) form as

$$H^{\text{PW}} = \sum_{\bar{i}} (\varepsilon_{\bar{i}} + V_{i\bar{i}}^p) N_{\bar{i}} + \sum_{i \neq \bar{j}} V_{i\bar{i}j\bar{j}}^p A_i^\dagger A_{\bar{j}} + \sum_{i \neq \bar{j}} V_{i\bar{i}j\bar{j}}^m N_{\bar{i}} N_{\bar{j}}, \quad (7)$$

$$\varepsilon_{\bar{i}} \equiv 2\varepsilon_i = \varepsilon_i + \varepsilon_{\bar{i}}, \quad (8)$$

$$V_{i\bar{j}}^p \equiv V_{i\bar{i}j\bar{j}}, \quad (9)$$

$$V_{i\bar{j}}^m \equiv V_{ijij} + V_{i\bar{j}i\bar{j}} + V_{i\bar{j}j\bar{i}} + V_{i\bar{i}j\bar{j}}. \quad (10)$$

More details on this derivation are provided in the Supplementary Information. The factor 1/2 in Eq. (6) is sometimes omitted (as in our earlier work [24]), but is retained here to emphasize the interpretation of  $N_{\bar{i}}$  as the occupation number of a pair degree of freedom.

The paired-neutron operators satisfy bosonic commutation relations, as detailed in e.g. [24, 25, 46], but multiple occupancy of the same pair is forbidden, hence the term hard-core boson (HCB). A key advantage of the HCB representation—beyond the qubit reduction—is the elimination of non-local Jordan–Wigner strings when mapping to Pauli operators. From Jordan–Wigner mappings,

Pauli- $Z$  terms appear to maintain the anti-commutation relations of the fermionic operators. In some literature, these Pauli- $Z$  terms are omitted, which is referred to as qubit excitation in Refs. [48, 49], as a hardware-efficient mapping. Those Pauli- $Z$  terms naturally cancel out in the pair-wise form of the Hamiltonian. Hence, one can map the Hamiltonian to the Pauli operators into simple forms as Eq. (1).

All the terms fall into two categories: One is diagonal terms in the computational basis,  $\{I, Z, ZZ\}$ , measurable directly, and the other is off-diagonal terms,  $\{XX, YY\}$ , requiring additional measurement circuits. The measurement strategies are described later in this section.

### ansatze

The ansatz plays a central role in quantum algorithms, both in the NISQ and FTQC regimes. In practice, the ansatz (i.e., the trial wave function) must satisfy two requirements: (1) it should be implementable on available quantum hardware, and (2) it should be expressive enough to approximate, e.g., the true ground state with high fidelity.

In this work, we employ the pair unitary coupled cluster doubles (pUCCD) ansatz for even-even multi-neutron systems. As shown in Fig. 1, pUCCD provides ground-state energies comparable in accuracy to doubly occupied configuration interaction (DOCI) method, while requiring far fewer parameters.

The pUCCD ansatz is a quantum version of the pair coupled cluster doubles method. A seminal work on the pUCCD ansatz in the context of quantum computing is found in Ref. [25], where strategies for measurement and post-selection were also proposed. In chemistry, pUCCD has been successfully applied to systems of paired electrons with spin up and spin down [25–27].

A related study by Sarma et al. [16] considered oxygen isotopes in the  $sd$  shell on a trapped-ion quantum computer, IonQ Aria, using a variant of unitary coupled cluster doubles (UCCD) ansatz applied only to time-reversal nucleon pairs (denoted UCCD ( $\nu = 0$ )) in the following where  $\nu$  is the seniority).

Although formally equivalent to DOCI, their implementation yielded ground-state errors of 3–13% relative to FCI, depending on the isotope. One limitation arises from the scaling of circuit parameters: the number of Givens rotations required grows rapidly with system size, making direct application to heavier isotopes impractical.

By contrast, the pUCCD ansatz with a single Trotter step scales more favorably, as

$$N_{\text{param}} = N_{\text{occ.}}(N_q - N_{\text{occ.}}), \quad (11)$$

where  $N_{\text{occ.}}$  is the number of occupied pairs and  $N_q$  the number of qubits in the HCB representation. This scaling is significantly milder than that of UCCD ( $\nu = 0$ ), as summarized in Table III. Note that the FCI dimension is also shown in the table for reference, and these show the

number of configurations in the so-called M-scheme, i.e. the basis states are labeled by the sum of the  $j_z$  values of the single-particle states. For even number of neutrons, all the states with different total angular momentum  $J$  are included in the  $M = 0$  subspace leading to the FCI dimension shown in the table.

The pUCCD ansatz is expressed as

$$|\psi_{\text{pUCCD}}\rangle = \exp(T - T^\dagger) |\text{ref.}\rangle \equiv U |\text{ref.}\rangle, \quad (12)$$

where  $T$  is the cluster operator and  $|\text{ref.}\rangle$  is a reference state. For paired-neutron excitations, the unitary operator takes the form

$$U = \exp \left[ \sum_{ph} t_h^p (A_p^\dagger A_h - A_h^\dagger A_p) \right], \quad (13)$$

with  $t_h^p$  the cluster amplitudes, and  $A_p^\dagger, A_h$  the pair creation and annihilation operators, Eqs. (4) and (5), respectively. The indices  $p$  and  $h$  denote the particle and hole states, respectively. Mapping to Pauli operators yields

$$U_{\text{qubit}} = \exp \left[ \sum_{ph} \frac{it_h^p}{2} (X_p Y_h - Y_p X_h) \right], \quad (14)$$

$$\approx \prod_{ph} \exp \left[ \frac{it_h^p}{2} (X_p Y_h - Y_p X_h) \right], \quad (15)$$

where the last expression corresponds to a first-order Trotter approximation with a single step, which we adopt in this work.

Each factor in Eq. (15) is equivalent to a Givens rotation acting on qubits  $p$  and  $h$ :

$$G(\theta) = \begin{pmatrix} 1 & 0 & 0 & 0 \\ 0 & \cos(\theta/2) & -\sin(\theta/2) & 0 \\ 0 & \sin(\theta/2) & \cos(\theta/2) & 0 \\ 0 & 0 & 0 & 1 \end{pmatrix} \quad (16)$$

Thus, the pUCCD ansatz can be implemented using relatively shallow circuits.

Fig. 4 illustrates two circuit layouts for preparing the pUCCD ansatz, taking  $^{20}\text{O}$  nucleus as an example. **a.** pUCCD (GS): optimized for devices with limited connectivity (e.g., IBM heavy-hexagon architectures), using Givens rotations followed by SWAP gates (GS) [25]. The basic idea behind the circuit is detailed in Ref. [50]. **b.** pUCCD (G): one realization for all-to-all connectivity (e.g., trapped-ion devices), requiring only Givens rotations.

While pUCCD (GS) has a nearly unique circuit layout, pUCCD (G) admits many realizations depending on the choice of initial configuration and ordering of Givens rotations. We therefore present simulator results for pUCCD (G) as distributions over multiple circuit realizations. In what follows, we use a single deterministic realization for both pUCCD (GS) and pUCCD (G) unless otherwise noted. Adaptive strategies such as orbital optimization or ansatz refinement could further enhance accuracy, but are left for future work.

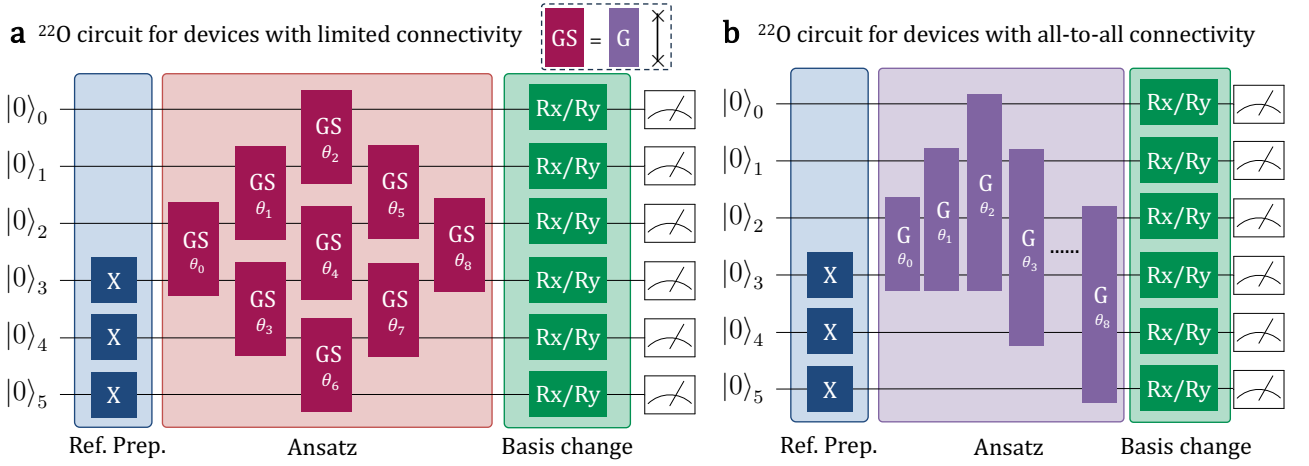


FIG. 4. **Quantum circuits for pUCCD ansatz.** Sketched quantum circuits for preparing the pUCCD ansatz taking  $^{20}\text{O}$  as an example. **a.** Circuit layout suitable for devices with heavy-hexagon connectivity. **b.** Circuit layout for all-to-all connectivity. First, the reference state is prepared by applying  $X$  gates to qubits. Then, Givens rotations (Eq. (16)) are applied to take into account particle-hole excitations of nucleon pairs. Single-qubit rotations are applied as needed prior to measuring Hamiltonian expectation values.

TABLE III. **Dimension and number of parameters in ansatz.** Comparison of FCI dimension and the number of parameters in the circuits for UCCD ( $\nu = 0$ ) [16] and pUCCD ansatz. The UCCD ( $\nu = 0$ ) is unitary coupled cluster doubles ansatz where the configurations are restricted to zero-seniority configurations. The rightmost column means the pair unitary coupled cluster doubles ansatz with a single Trotter step.

| Nucleus                             | FCI (M=0) | UCCD ( $\nu = 0$ ) | pUCCD |
|-------------------------------------|-----------|--------------------|-------|
| $^{18}\text{O}$ , $^{26}\text{O}$   | 14        | 5                  | 5     |
| $^{20}\text{O}$ , $^{24}\text{O}$   | 81        | 14                 | 8     |
| $^{22}\text{O}$                     | 142       | 19                 | 9     |
| $^{42}\text{Ca}$ , $^{58}\text{Ca}$ | 30        | 9                  | 9     |
| $^{44}\text{Ca}$ , $^{56}\text{Ca}$ | 565       | 44                 | 16    |
| $^{46}\text{Ca}$ , $^{54}\text{Ca}$ | 3952      | 119                | 21    |
| $^{48}\text{Ca}$ , $^{52}\text{Ca}$ | 12,022    | 209                | 24    |
| $^{50}\text{Ca}$                    | 17,276    | 251                | 25    |
| $^{58}\text{Ni}$ , $^{76}\text{Ni}$ | 19        | 10                 | 10    |
| $^{60}\text{Ni}$ , $^{74}\text{Ni}$ | 365       | 54                 | 18    |
| $^{62}\text{Ni}$ , $^{72}\text{Ni}$ | 3,103     | 164                | 24    |
| $^{64}\text{Ni}$ , $^{70}\text{Ni}$ | 12,240    | 329                | 28    |
| $^{66}\text{Ni}$ , $^{68}\text{Ni}$ | 23,884    | 461                | 30    |

### Implementation of Givens rotation gates

To construct the pUCCD ansatz circuits (Fig. 4) and to perform basis rotations for diagonalizing the  $XX+YY$  terms, it is necessary to implement Givens rotation gates.

Several approaches are known in literature. In this work, we examined the following three methods:

1. Magic-gate method (Ref. [51]) - implements Givens rotation using a sequence of "magic" gates.
2.  $\sqrt{\text{SWAP}}$ -based method (Ref. [50]) - uses  $\sqrt{\text{SWAP}}$  gates to construct the Givens rotation.

3. Controlled- $R_y$  method (Ref. [52]) - equivalent to a breakdown of controlled- $R_y$  followed by CNOT gates.

At the raw circuit level, these methods require 2, 4, and 3 CNOT gates per Givens rotation, respectively. However, we found the number of CNOTs for the transpiled circuits are equivalent to each other. As a result, the total numbers of CNOTs in the for pUCCD (GS) and pUCCD (G) ansatzes scale as  $3N_G$  and  $2N_G$ , where  $N_G$  is the number of Givens rotations in the ansatz.

Quantum circuits submitted to the hardware are transformed to native gate sets of the adopted hardware. For the RIKEN-Quantinuum's Reimei device, CNOT gates are to be transpiled to another two-qubit gate, the so-called ZZPhase gate,  $\exp(-i\pi\alpha/2(Z_p \otimes Z_q))$ . Here we follow the notation of pytket [53, 54], i.e., angle parameter is given in the unit of  $\pi/2$ . Indeed, the number of ZZPhase gates for the compiled pUCCD (G) ansatz became twice the number of Givens rotations listed in Tab. III.

### Measurement of energy expectation values

In this work, the parameters of the pUCCD ansatz were optimized on statevector simulators using the Adam optimizer using PennyLane [55]. This is still an idealized setting, but good starting point to evaluate the ansatz quality and measurement strategies. The strategy to optimize the ansatz circuit on a real device is left as a future issue. Optimization directly on quantum hardware remains an open problem, for which gradient-free sequential approaches [56] may offer a promising path.

Once the ansatz circuit is prepared, the next task is



to evaluate the expectation value of the Hamiltonian. For noise-free simulations, one does not need to care about the measurement strategy, but it is crucial point to be considered for noisy simulations and experiments on hardware.

Diagonal terms in the computational basis, i.e., operators involving  $\{I, Z, ZZ\}$ , can be obtained by measuring the ansatz circuit in the computational basis. In this case, post-selection techniques is naturally applicable: bitstrings violating the particle number of the target system are discarded.

In contrast, non-diagonal terms  $\{XX, YY\}$  require additional circuits. This is especially costly on hardware with limited connectivity, where extra SWAP gates increase circuit depth and accumulate noise. We therefore considered two measurement strategies: First one, referred to as the ‘‘Hadamard’’ method in Results section, is the straightforward approach using Hadamard gates. The ansatz is followed by Hadamard gates on each qubit, after which measurements are taken in the computational basis. This allows direct access to all  $X_p X_q$  expectation values. Since  $XX$  and  $YY$  terms contribute equally to the energy,  $\langle YY \rangle$  are evaluated by doubling  $\langle XX \rangle$  values. While straightforward, this method does not preserve particle-number symmetry, limiting the use of post-selection. Note that one can consider applying the so-called computational basis sampling method [57]. The second strategy is to be referred to as basis rotation (BasisRot), diagonalizing  $XX + YY$  terms prior to measurement [25, 29]:

$$\begin{aligned} \langle \psi | X_p X_q + Y_p Y_q | \psi \rangle \\ = \langle \psi | \mathcal{U}_{p,q}(\pi/4) (Z_p - Z_q) \mathcal{U}_{p,q}^\dagger(\pi/4) | \psi \rangle, \end{aligned} \quad (17)$$

where  $\mathcal{U}_{p,q}(\theta)$  is a Givens rotation  $G(2\theta)$ , Eq. (16), applied to qubits  $p$  and  $q$ . Following Ref. [29], the required terms can be grouped such that only  $2\lfloor N_q/2 \rfloor$  additional circuits are needed to measure all the  $XX + YY$  terms, where  $N_q$  is the number of qubits. On devices with all-to-all connectivity, SWAP gates for this arrangement are not strictly necessary; however, we employed them to make comparison with the H-gate method rather straightforward. Importantly, this strategy preserves particle-number symmetry, enabling effective post-selection.

It should be noted that energies estimated from separately measured terms is not guaranteed to be lower than the true ground state energy. are generally non-variational, even with post-selection. Since diagonal and off-diagonal contributions are measured independently, their sum is not guaranteed to remain below the true ground-state energy.

#### Remarks on statistical uncertainty of hardware results

To quantify statistical uncertainties in hardware results, we applied a bootstrapping analysis. As an illustration, Fig. 5, shows the distribution of the ground-state

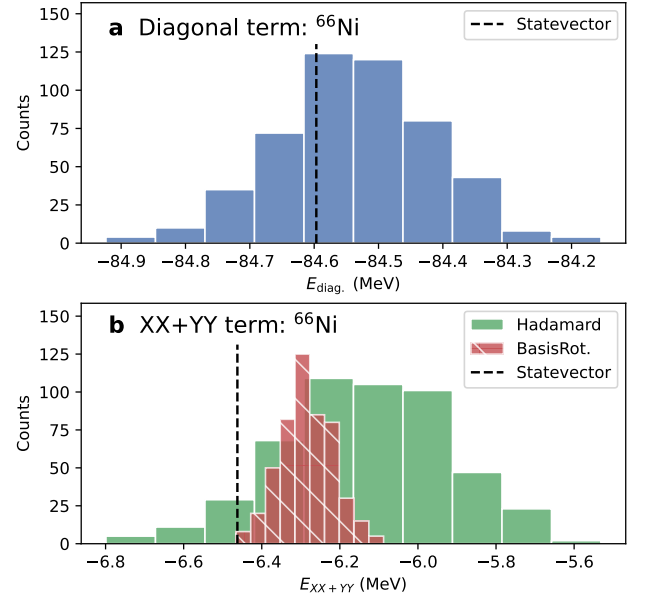


FIG. 5. **Statistical uncertainty of hardware results for <sup>66</sup>Ni.** **a** diagonal terms. **b**  $XX+YY$  terms evaluated by two measurement strategies: Hadamard (green) and basis rotation (red with hatching). The distributions are obtained by bootstrap, i.e., resampling the raw data 500 times. The vertical dashed line shows the ideal statevector simulation result.

energy of <sup>66</sup>Ni obtained by resampling the data 500 times. The energy is separated into contributions from diagonal terms (top panel) and  $XX + YY$  terms (bottom panel). Vertical dashed lines indicate the corresponding noise-free statevector results for comparison.

The accuracy on the diagonal term depends primarily on occupation numbers, while the  $XX + YY$  terms are contribution is more sensitive to both occupation numbers and relative phases between configurations. As shown in the lower panel of Fig. 5, the distribution obtained using the Hadamard method is noticeably broader than that obtained with basis rotations. This indicates that the basis-rotation strategy is more robust against statistical noise, especially when the number of measurement shots is limited.

We emphasize, however, that this analysis does not account for systematic errors inherent to the Reimei device. Therefore, our results do not imply that the basis-rotation method always outperforms the Hadamard method in practice. Nonetheless, the observed trends (see also Fig. 2) suggest that basis rotations tend to yield more stable estimates of energy expectation values for the systems studied here.

#### Hardware information

The experiments on the Reimei trapped-ion quantum computer were carried out via the Quantinuum Nexus [28] platform. Table IV summarizes the calibra-

tion data of the Reimei device, which were obtained on 2025-05-09. The reported metrics include single- and two-qubit gate errors, SPAM (state preparation and measurement) errors, crosstalk, and memory error rates. These parameters provide a baseline for evaluating the quality of quantum circuits executed on the device. In particular, the relatively low one- and two-qubit gate error rates, combined with the all-to-all connectivity of trapped-ion hardware, enable the accurate implementation of the pUCCD ansatz circuits described in this work.

TABLE IV. **Calibration data of the Reimei device** The values are from data on 2025-05-09 via the Quantinuum's Nexus [28] platform.

| Error type                 | Value                 | Uncertainty           |
|----------------------------|-----------------------|-----------------------|
| One-qubit gate error $P_1$ | $4.22 \times 10^{-5}$ | $5.23 \times 10^{-6}$ |
| Two-qubit gate error $P_2$ | $1.39 \times 10^{-3}$ | $5.92 \times 10^{-5}$ |
| SPAM error (0)             | $2.73 \times 10^{-3}$ | $1.57 \times 10^{-4}$ |
| SPAM error (1)             | $5.25 \times 10^{-3}$ | $2.18 \times 10^{-4}$ |
| Crosstalk error            | $3.21 \times 10^{-5}$ | $1.89 \times 10^{-6}$ |
| Memory error               | $2.83 \times 10^{-4}$ | $2.32 \times 10^{-5}$ |

## DATA AVAILABILITY

The data presented in this manuscript are available from the GitHub repository [58].

## CODE AVAILABILITY

One can reproduce the results of this work (within uncertainties due to randomness) by the code available at the GitHub repository [58]. For classical computations, the data can be reproduced by using the NuclearToolkit.jl package [40, 41] with the interaction files available through KSHELL [38, 39]. We utilized the Qiskit [59], PennyLane [55], and pytket [53, 54] for quantum computations. Experiments on the Reimei device were carried out using the Quantinuum's Nexus [28] platform.

- 
- [1] N. Yoshioka, T. Okubo, Y. Suzuki, Y. Koizumi, and W. Mizukami, *npj Quantum Information* **10**, 45 (2024).
  - [2] A. Peruzzo, J. McClean, P. Shadbolt, M.-H. Yung, X.-Q. Zhou, P. J. Love, A. Aspuru-Guzik, and J. L. O'Brien, *Nat. Commun.* **5**, 4213 (2014).
  - [3] K. Bharti, A. Cervera-Lierta, T. H. Kyaw, T. Haug, S. Alperin-Lea, A. Anand, M. Degroote, H. Heimonen, J. S. Kottmann, T. Menke, W.-K. Mok, S. Sim, L.-C. Kwek, and A. Aspuru-Guzik, *Rev. Mod. Phys.* **94**, 015004 (2022).
  - [4] M. Larocca, S. Thanasilp, S. Wang, K. Sharma, J. Biamonte, P. J. Coles, L. Cincio, J. R. McClean, Z. Holmes, and M. Cerezo, *Nature Reviews Physics* **7**, 174 (2025).
  - [5] A. Katarbwa, K. Gratsea, A. Caesura, and P. D. Johnson, *PRX Quantum* **5**, 020101 (2024).
  - [6] A. Y. Kitaev, *Quantum measurements and the abelian stabilizer problem* (1995), [arXiv:quant-ph/9511026 \[quant-ph\]](#).
  - [7] S.-J. Ran, *Phys. Rev. A* **101**, 032310 (2020).
  - [8] T. Felser, S. Notarnicola, and S. Montangero, *Phys. Rev. Lett.* **126**, 170603 (2021).
  - [9] D. Malz, G. Styliaris, Z.-Y. Wei, and J. I. Cirac, *Phys. Rev. Lett.* **132**, 040404 (2024).
  - [10] E. F. Dumitrescu, A. J. McCaskey, G. Hagen, G. R. Jansen, T. D. Morris, T. Papenbrock, R. C. Pooser, D. J. Dean, and P. Lougovski, *Phys. Rev. Lett.* **120**, 210501 (2018).
  - [11] D. Lacroix, *Phys. Rev. Lett.* **125**, 230502 (2020).
  - [12] A. Pérez-Obiol, A. M. Romero, J. Menéndez, A. Rios, A. García-Sáez, and B. Juliá-Díaz, *Sci. Rep.* **13**, 12291 (2023).
  - [13] J. E. García-Ramos, A. Sáiz, J. M. Arias, L. Lamata, and P. Pérez-Fernández, *Advanced Quantum Technologies* **n/a**, 2300219 (2023).
  - [14] Savage, Martin J., *EPJ Web Conf.* **296**, 01025 (2024).
  - [15] O. Kiss, M. Grossi, P. Lougovski, F. Sanchez, S. Vallecorsa, and T. Papenbrock, *Phys. Rev. C* **106**, 034325 (2022).
  - [16] C. Sarma, O. Di Matteo, A. Abhishek, and P. C. Srivastava, *Phys. Rev. C* **108**, 064305 (2023).
  - [17] H. R. Grimsley, S. E. Economou, E. Barnes, and N. J. Mayhall, *Nature Communications* **10**, 3007 (2019).
  - [18] T. Otsuka, T. Suzuki, R. Fujimoto, H. Grawe, and Y. Akaishi, *Phys. Rev. Lett.* **95**, 232502 (2005).
  - [19] K. Hebeler, *Physics Reports* **890**, 1 (2021), three-nucleon forces: Implementation and applications to atomic nuclei and dense matter.
  - [20] C. Gu, Z. H. Sun, G. Hagen, and T. Papenbrock, *Phys. Rev. C* **108**, 054309 (2023).
  - [21] V. Bettaque and B. Swingle, *Quantum* **8**, 1362 (2024).
  - [22] W.-Y. Liu, S.-J. Du, R. Peng, J. Gray, and G. K.-L. Chan, *Phys. Rev. Lett.* **133**, 260404 (2024).
  - [23] S. Lu, M. Kanász-Nagy, I. Kukuljan, and J. I. Cirac, *Phys. Rev. A* **111**, 032409 (2025).
  - [24] S. Yoshida, T. Sato, T. Ogata, T. Naito, and M. Kimura, *Phys. Rev. C* **109**, 064305 (2024).
  - [25] V. E. Elfving, M. Millaruelo, J. A. Gámez, and C. Gogolin, *Phys. Rev. A* **103**, 032605 (2021).
  - [26] T. E. O'Brien, G. Anselmetti, F. Gkritis, V. E. Elfving, S. Polla, W. J. Huggins, O. Oumarou, K. Kechedzhi, D. Abanin, R. Acharya, I. Aleiner, R. Allen, T. I. Andersen, K. Anderson, M. Ansmann, F. Arute, K. Arya, A. Asfaw, J. Atalaya, J. C. Bardin, A. Bengtsson, G. Bortoli, A. Bourassa, J. Bovaird, L. Brill, M. Broughton, B. Buckley, D. A. Buell, T. Burger, B. Burkett, N. Bushnell, J. Campero, Z. Chen, B. Chiaro, D. Chik, J. Cogan, R. Collins, P. Conner, W. Courtney, A. L. Crook, B. Curtin, D. M. Debroy, S. Demura, I. Drozdov, A. Dunsworth, C. Erickson, L. Faoro, E. Farhi, R. Fatemi, V. S. Ferreira, L. Flores Burgos, E. Fo-

- rati, A. G. Fowler, B. Foxen, W. Jiang, C. Gidney, D. Gilboa, M. Giustina, R. Gosula, A. Grajales Dau, J. A. Gross, S. Habegger, M. C. Hamilton, M. Hansen, M. P. Harrigan, S. D. Harrington, P. Heu, M. R. Hoffmann, S. Hong, T. Huang, A. Huff, L. B. Ioffe, S. V. Isakov, J. Iveland, E. Jeffrey, Z. Jiang, C. Jones, P. Juhas, D. Kafri, T. Khattar, M. Khezri, M. Kieferová, S. Kim, P. V. Klimov, A. R. Klots, A. N. Korotkov, F. Kostritsa, J. M. Kreikebaum, D. Landhuis, P. Laptev, K. M. Lau, L. Laws, J. Lee, K. Lee, B. J. Lester, A. T. Lill, W. Liu, W. P. Livingston, A. Locharla, F. D. Malone, S. Mandrà, O. Martin, S. Martin, J. R. McClean, T. McCourt, M. McEwen, X. Mi, A. Mieszala, K. C. Miao, M. Mohseni, S. Montazeri, A. Morvan, R. Movassagh, W. Mruczkiewicz, O. Naaman, M. Neeley, C. Neill, A. Nersisyan, M. Newman, J. H. Ng, A. Nguyen, M. Nguyen, M. Y. Niu, S. Omonije, A. Opremcak, A. Petukhov, R. Potter, L. P. Pryadko, C. Quintana, C. Rocque, P. Roushan, N. Saei, D. Sank, K. Sankaragomathi, K. J. Satzinger, H. F. Schurkus, C. Schuster, M. J. Shearn, A. Shorter, N. Shutty, V. Shvarts, J. Skrzynny, W. C. Smith, R. D. Somma, G. Sterling, D. Strain, M. Szalay, D. Thor, A. Torres, G. Vidal, B. Villalonga, C. Vollgraff Heidweiller, T. White, B. W. K. Woo, C. Xing, Z. J. Yao, P. Yeh, J. Yoo, G. Young, A. Zalcman, Y. Zhang, N. Zhu, N. Zobrist, D. Bacon, S. Boixo, Y. Chen, J. Hilton, J. Kelly, E. Lucero, A. Megrant, H. Neven, V. Smelyanskiy, C. Gogolin, R. Babbush, and N. C. Rubin, *Nature Physics* **19**, 1787 (2023).
- [27] L. Zhao, J. Goings, K. Shin, W. Kyoung, J. I. Fuks, J.-K. Kevin Rhee, Y. M. Rhee, K. Wright, J. Nguyen, J. Kim, and S. Johri, *npj Quantum Information* **9**, 60 (2023).
- [28] *Quantinuum nexus* (2024).
- [29] G. A. Quantum and Collaborators, *Science* **369**, 1084 (2020).
- [30] H. Hergert, *Frontiers in Physics* **8**, 379 (2020).
- [31] M. Honma, T. Otsuka, T. Mizusaki, and M. Hjorth-Jensen, *Phys. Rev. C* **80**, 064323 (2009).
- [32] A. Pérez-Obiol, S. Masot-Llima, A. M. Romero, J. Menéndez, A. Rios, A. García-Sáez, and B. Juliá-Díaz, *Entropy-driven entanglement forging* (2024), [arXiv:2409.04510 \[quant-ph\]](https://arxiv.org/abs/2409.04510).
- [33] N. H. Stair, R. Huang, and F. A. Evangelista, *Journal of Chemical Theory and Computation* **16**, 2236 (2020).
- [34] C. L. Cortes and S. K. Gray, *Phys. Rev. A* **105**, 022417 (2022).
- [35] K. Kanno, M. Kohda, R. Imai, S. Koh, K. Mitarai, W. Mizukami, and Y. O. Nakagawa, *Quantum-selected configuration interaction: classical diagonalization of hamiltonians in subspaces selected by quantum computers* (2023), [arXiv:2302.11320 \[quant-ph\]](https://arxiv.org/abs/2302.11320).
- [36] J. Robledo-Moreno, M. Motta, H. Haas, A. Javadi-Abhari, P. Jurcevic, W. Kirby, S. Martiel, K. Sharma, S. Sharma, T. Shirakawa, I. Sitdikov, R.-Y. Sun, K. J. Sung, M. Takita, M. C. Tran, S. Yunoki, and A. Mezzacapo, *Science Advances* **11**, eadu9991 (2025), <https://www.science.org/doi/pdf/10.1126/sciadv.adu9991>.
- [37] N. Yoshioka, M. Amico, W. Kirby, P. Jurcevic, A. Dutt, B. Fuller, S. Garion, H. Haas, I. Hamamura, A. Ivrii, R. Majumdar, Z. Mineev, M. Motta, B. Pokharel, P. Rivero, K. Sharma, C. J. Wood, A. Javadi-Abhari, and A. Mezzacapo, *Nature Communications* **16**, 5014 (2025).
- [38] N. Shimizu, Nuclear shell-model code for massive parallel computation, “KSHELL” (2013), [arXiv:1310.5431](https://arxiv.org/abs/1310.5431).
- [39] N. Shimizu, T. Mizusaki, Y. Utsuno, and Y. Tsunoda, *Comput. Phys. Commun.* **244**, 372 (2019).
- [40] S. Yoshida, *Journal of Open Source Software* **7**, 4694 (2022).
- [41] S. Yoshida, <https://github.com/SotaYoshida/NuclearToolkit.jl>.
- [42] B. A. Brown and W. A. Richter, *Phys. Rev. C* **74**, 034315 (2006).
- [43] M. Honma, T. Otsuka, B. A. Brown, and T. Mizusaki, *Eur. Phys. J. A* **25**, 499 (2005).
- [44] A. Volya, B. Brown, and V. Zelevinsky, *Physics Letters B* **509**, 37 (2001).
- [45] T. M. Henderson, G. E. Scuseria, J. Dukelsky, A. Signoracci, and T. Duguet, *Phys. Rev. C* **89**, 054305 (2014).
- [46] T. M. Henderson, I. W. Bulik, and G. E. Scuseria, *The Journal of Chemical Physics* **142**, 214116 (2015).
- [47] Y. Qiu, T. M. Henderson, T. Duguet, and G. E. Scuseria, *Phys. Rev. C* **99**, 044301 (2019).
- [48] Y. S. Yordanov, D. R. M. Arvidsson-Shukur, and C. H. W. Barnes, *Phys. Rev. A* **102**, 062612 (2020).
- [49] Y. S. Yordanov, V. Armaos, C. H. W. Barnes, and D. R. M. Arvidsson-Shukur, *Communications Physics* **4**, 228 (2021).
- [50] I. D. Kivlichan, J. McClean, N. Wiebe, C. Gidney, A. Aspuru-Guzik, G. K.-L. Chan, and R. Babbush, *Phys. Rev. Lett.* **120**, 110501 (2018).
- [51] F. Vatan and C. Williams, *Phys. Rev. A* **69**, 032315 (2004).
- [52] J. M. Arrazola, O. Di Matteo, N. Quesada, S. Jahangiri, A. Delgado, and N. Killoran, *Quantum* **6**, 742 (2022).
- [53] S. Sivarajah, S. Dilkes, A. Cowtan, W. Simmons, A. Edgington, and R. Duncan, *Quantum Science and Technology* **6**, 014003 (2020).
- [54] *pytket-quantinuum*.
- [55] V. Bergholm, J. Izaac, M. Schuld, C. Gogolin, S. Ahmed, V. Ajith, M. S. Alam, G. Alonso-Linares, B. Akash-Narayanan, A. Asadi, J. M. Arrazola, U. Azad, S. Banning, C. Blank, T. R. Bromley, B. A. Cordier, J. Ceroni, A. Delgado, O. D. Matteo, A. Dusko, T. Garg, D. Guala, A. Hayes, R. Hill, A. Ijaz, T. Isaacson, D. Ittah, S. Jahangiri, P. Jain, E. Jiang, A. Khandelwal, K. Kottmann, R. A. Lang, C. Lee, T. Loke, A. Lowe, K. McKiernan, J. J. Meyer, J. A. Montañez-Barrera, R. Moyard, Z. Niu, L. J. O’Riordan, S. Oud, A. Panigrahi, C.-Y. Park, D. Polatajko, N. Quesada, C. Roberts, N. Sá, I. Schoch, B. Shi, S. Shu, S. Sim, A. Singh, I. Strandberg, J. Soni, A. Száva, S. Thabet, R. A. Vargas-Hernández, T. Vincent, N. Vitucci, M. Weber, D. Wierichs, R. Wiersema, M. Willmann, V. Wong, S. Zhang, and N. Killoran, *Penylane: Automatic differentiation of hybrid quantum-classical computations* (2022), [arXiv:1811.04968 \[quant-ph\]](https://arxiv.org/abs/1811.04968).
- [56] K. M. Nakanishi, K. Fujii, and S. Todo, *Phys. Rev. Res.* **2**, 043158 (2020).
- [57] M. Kohda, R. Imai, K. Kanno, K. Mitarai, W. Mizukami, and Y. O. Nakagawa, *Phys. Rev. Res.* **4**, 033173 (2022).
- [58] *Repository to be opened*.
- [59] Qiskit contributors, *Qiskit: An open-source framework for quantum computing* (2023).

# **ACKNOWLEDGMENTS**

This research was supported in part by JSPS Grant-in-Aid for Scientific Research (Grant Nos. JP22K14030, JP25H01511, JP25K01688), JST COI-NEXT (Grant No. JPMJPF2221), MEXT Q-LEAP (Grant No. JPMXS0118067246), and RIKEN TRIP initiative (Nuclear Transmutation). This paper is based on results obtained from a project, JPNP20017, commissioned by the New Energy and Industrial Technology Development Organization (NEDO).

# **AUTHOR CONTRIBUTIONS**

S.Y. conceived the idea of the project, developed the framework and the code, and performed the simulations and analyses. T.S. and T.O. contributed to the design of the ansatz and of the quantum circuits from chemical background. M.K. supervised the project. All authors contributed to verifying the results and writing the manuscript.

## SUPPLEMENTARY INFORMATION

### I. DERIVATION OF HARD-CORE-BOSON FORM OF THE HAMILTONIAN

Here we provide the detailed derivation of the pair-wise Hamiltonians for the systems of interest, corresponding to Eq. (3) of the main text. Starting from the fermionic Hamiltonian with up to two-body interactions, we introduced time-reversal pairs  $(i, \bar{i})$  and defined pair creation, annihilation, and number operators in Eqs. (5)–(6).

After reorganizing terms and discarding those irrelevant within the zero-seniority space, the Hamiltonian reduces to the following forms:

$$\sum_i \varepsilon_i a_i^\dagger a_i = \sum_{i < 0} (\varepsilon_i a_i^\dagger a_i + \varepsilon_{\bar{i}} a_{\bar{i}}^\dagger a_{\bar{i}}) = \sum_{\tilde{i}} \varepsilon_{\tilde{i}} N_{\tilde{i}}, \quad (18)$$

$$\frac{1}{4} \sum_{ijkl} V_{ijkl} a_i^\dagger a_j^\dagger a_k a_l = \frac{1}{4} \sum_{ij} V_{i\bar{i}j\bar{j}} a_i^\dagger a_{\bar{i}}^\dagger a_j a_{\bar{j}} + \frac{1}{4} \sum_{i,j \notin \{i,\bar{i}\}} V_{ijij} a_i^\dagger a_j^\dagger a_j a_i + (\text{irrelevant terms}), \quad (19)$$

$$\frac{1}{4} \sum_{i,j \in \{i,\bar{i}\}} V_{i\bar{i}j\bar{j}} a_i^\dagger a_{\bar{i}}^\dagger a_j a_{\bar{j}} = \frac{1}{4} \left( \sum_i V_{i\bar{i}i\bar{i}} a_i^\dagger a_{\bar{i}}^\dagger a_i a_{\bar{i}} + \sum_i V_{i\bar{i}i\bar{i}} a_i^\dagger a_{\bar{i}}^\dagger a_i a_{\bar{i}} \right) = \frac{1}{2} \sum_i V_{i\bar{i}i\bar{i}} a_i^\dagger a_{\bar{i}}^\dagger a_i a_{\bar{i}} = \sum_{i < 0} V_{i\bar{i}i\bar{i}} a_i^\dagger a_{\bar{i}}^\dagger a_i a_{\bar{i}}, \quad (20)$$

$$\frac{1}{4} \sum_{i,j \notin \{i,\bar{i}\}} V_{i\bar{i}j\bar{j}} a_i^\dagger a_{\bar{i}}^\dagger a_j a_{\bar{j}} = \sum_{i < 0} \sum_{j \notin \{i,\bar{i}\} < 0} V_{i\bar{i}j\bar{j}} a_i^\dagger a_{\bar{i}}^\dagger a_j a_{\bar{j}} = \sum_{i \neq j < 0} V_{i\bar{i}j\bar{j}} a_i^\dagger a_{\bar{i}}^\dagger a_j a_{\bar{j}}, \quad (21)$$

$$\frac{1}{4} \sum_{i,j \notin \{i,\bar{i}\}} V_{ijij} a_i^\dagger a_j^\dagger a_j a_i = \frac{1}{4} \sum_{i,j \notin \{i,\bar{i}\}} V_{ijij} n_i n_j = \sum_{i < 0} \sum_{j \notin \{i,\bar{i}\} < 0} (V_{ijij} + V_{i\bar{j}i\bar{j}}) n_i n_j = \frac{1}{2} \sum_{\tilde{i}\tilde{j}} V_{\tilde{i}\tilde{j}}^m n_{\tilde{i}} n_{\tilde{j}}, \quad (22)$$

where the indices  $i, j, k, l$  denote a Fermionic single-particle states having  $\{n, l, j, j_z, t_z\}$  quanta. The  $\tilde{i}, \tilde{j}$  represent pair-wise basis states obtained by folding single-particle states  $i$  and  $\bar{i}$  (the time-reversed partner).

### II. UNCERTAINTY BANDS IN FIGURE 1

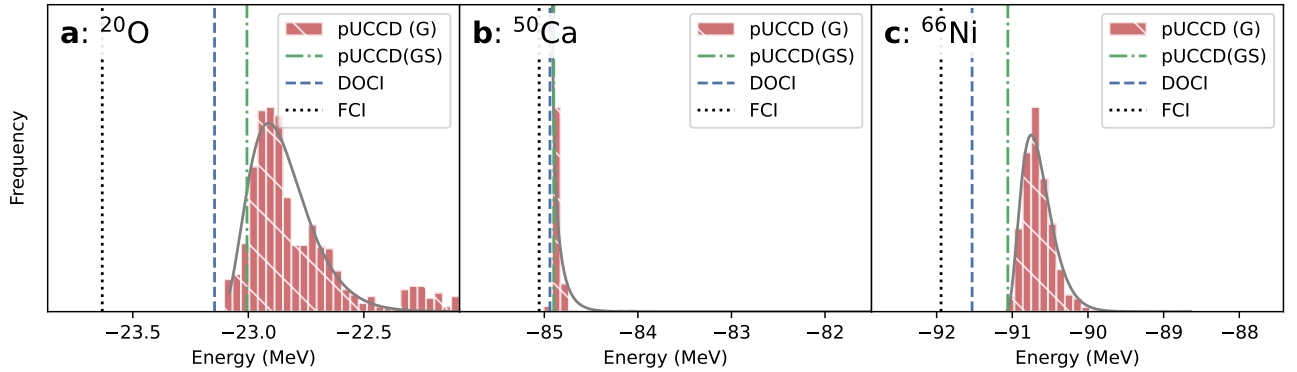


FIG. 6. **Uncertainty estimation for pUCCD (G) results.** Sampled possible realization of ansatz is fitted by a Gamma distribution for the pUCCD results of **a**  $^{20}\text{O}$ , **b**  $^{50}\text{Ca}$  and **c**  $^{66}\text{Ni}$ .

The pUCCD (G) ansatz can be realized in many different circuit layouts due to all-to-all connectivity. The number of possible circuits grows combinatorially with system size (e.g. for  $^{50}\text{Ca}$ , 252 possible reference states and 25! permutations of Givens rotations). Exhaustive sampling is thus impractical.

To estimate uncertainties, we generated 1,000 random circuits per nucleus, varying both the initial occupied qubits and the ordering of Givens rotations. The resulting energy distributions (examples shown in Fig. 6 for  $^{20}\text{O}$ ,  $^{50}\text{Ca}$ , and  $^{66}\text{Ni}$ ) are asymmetric but well approximated by a Gamma distribution. To ensure physical plausibility, the lower bound of the distribution was set to the lowest energy encountered in the samples, thereby avoiding unphysical assignment of energies below DOCI.

The fitted Gamma distributions were then used to construct the shaded uncertainty bands in Fig. 1 of the main text. We note that the pUCCD (GS) ansatz typically yields results close to the optimal edge of the pUCCD (G)



distribution, except for cases such as  $^{24}\text{O}$ ,  $^{50}\text{Ca}$ , and  $^{52}\text{Ca}$  where the qubit ordering or single-particle energy structure leads to less favorable initialization.

### III. RESULTS OF THE PUCCD (GS) ANSATZ ON IBM'S NOISY SIMULATOR

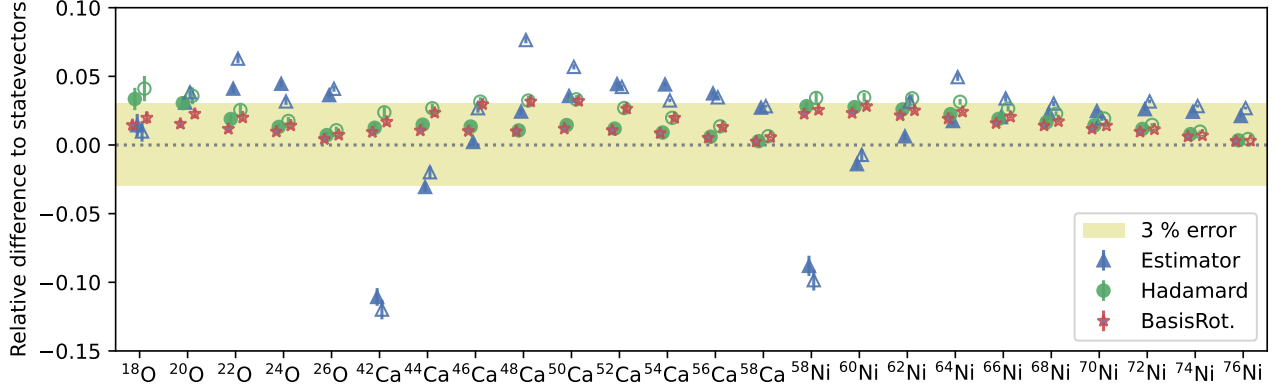


FIG. 7. **pUCCD results on IBM's noisy simulator.** Relative error to the ideal statevector simulation for the pUCCD ansatz. Closed markers correspond to Givens+SWAP (GS) circuits, open markers to Givens-only (G) circuits. Colors and markers indicate different measurement strategies as explained in the text. The shaded band denotes 3% deviation from the statevector results. Error bars show the standard deviation of 100 independent runs.

For completeness, we benchmark the pUCCD (GS) ansatz on IBM's noisy simulator (FakeTorino backend), which reflects the heavy-hexagon connectivity of IBM devices. In this setting, additional SWAP gates are required, increasing the CNOT count to  $3N_G$  (where  $N_G$  is the number of Givens rotations), compared to  $2N_G$  under all-to-all connectivity. Figure 7 summarizes the relative errors with respect to the ideal statevector simulations. Three measurement strategies were compared:

- **Estimator method** (blue triangles): direct expectation-value evaluation.
- **Hadamard method** (green circles): Hadamard gates are applied to access  $XX$  terms, with  $YY$  inferred by symmetry.
- **Basis-rotation method** (red stars):  $XX + YY$  terms are diagonalized via Givens rotations, enabling particle-number post-selection.

While all approaches yield errors within a few percent, the basis-rotation strategy consistently provides more stable results. In lighter nuclei, we observe a tendency to overestimate the binding energy with Estimator results. This behavior can be traced back to the measurement outcomes: bit strings corresponding to states with an incorrect particle number may occasionally appear. When such spurious configurations correspond to nuclei with a larger number of valence particles, they often yield lower expectation values of the Hamiltonian, i.e. artificial more bindings. As a result, the statistical averaging over these bit strings leads to an overbinding bias in light isotopes, where the relative contribution of such erroneous configurations is more pronounced.